ADVANCED MATERIALS TECHNOLOGIES
www.advmattechnol.de

Multimaterial Volumetric Printing of Silica-Based Glasses

Lorenzo Barbera, Jorge Madrid-Wolff, Roberto Emma, Kunal Masania, Antoine Boniface, Damien Loterie, Paul Delrot, Christophe Moser, and André R. Studart**

Silicate glasses have played a major role as structural and functional materials in human civilization since ancient Egypt. Despite their widespread use and importance in modern society, silica glasses with complex geometries are only fabricated in automated processes using 3D printing. Here, the volumetric printing of silica-based glasses with tunable multimaterial and microstructural control is reported. Volumetric printing enables complex shaping of photo-reactive resins in a few seconds using illumination techniques analogous to those employed for medical imaging. Particle-filled and phase-separating resins are used as photo-reactive feedstock that is quickly printed in 3D and subsequently converted into silica glasses through conventional heat treatment. Using rheology and imaging techniques, it is shown that the design of the resin is crucial to print complex geometries with high shape fidelity. The capabilities of the printing platform are demonstrated by fabricating a silica-based filtration device combining dense and porous glass with tunable compositions in a unique 3D structure.

1. Introduction

3D printing has enabled shaping of silica-based glasses into intricate geometries that are not accessible using conventional manufacturing technologies.[1–7] The unique shape complexity achieved by printing may find use in several prospective microfluidic, biomedical and optical applications.[8–10] Various approaches have been reported for the 3D printing of silica-based glasses. Most strategies involve either the deposition of molten glass at temperatures above 1000 °C[3,11] or the room-temperature printing of suspensions and resins loaded with inorganic precursors followed by a heat treatment procedure.[2,4,12] Printing at room temperature has been conducted using light- or extrusion-based techniques using silica particles[4,5,8,13–19] or metal alkoxides[2,6,9,10,12,20] as inorganic precursors. The extrusion-based methods benefit from their multimaterial capabilities, whereas light-based approaches are most suitable for printing intricate geometries at higher spatial resolutions. Importantly, most of the technologies demonstrated so far, rely on the layer-by-layer deposition of material, which is a relatively slow process that requires caution to prevent the formation of interlayer defects during fabrication.

The advent of volumetric printing techniques opened a new pathway for the fabrication of complex-shaped objects at high speeds circumventing the potential fabrication issues of layer-by-layer approaches. Inspired by computed tomography imaging, volumetric printing is a light-based additive manufacturing technology in which the entire object is printed at once by projecting light into a transparent photo-reactive resin placed in a rotating vat.[21–23] This novel printing approach has been recently exploited for the fabrication of heat-resistant silicon oxycarbide ceramics[24] and silica glass objects at high speeds with surface roughness down to 6 nanometers.[25] Such a low surface roughness makes this technology especially attractive for the 3D printing of complex-shaped optical components. Despite these enticing prospects, volumetric additive manufacturing of oxide glass is currently limited to the microscale and a single material composition.[25] Since most functional silica glasses require tuning of their physical and chemical properties through the introduction of other oxides into the composition, printing technologies for multicomponent glasses are crucial to broaden the possible application scenarios of these complex-shaped objects.

Multicomponent glasses can be printed by digital light processing using metal alkoxides as inorganic precursors in a photo-reactive resin.[2] In this approach, the metal alkoxides provide the cations of interest for the formation of multioxide glasses

L. Barbera, R. Emma, K. Masania[+], A. R. Studart
Complex Materials
Department of Materials
ETH Zürich
Zürich 8093, Switzerland
E-mail: andre.studart@mat.ethz.ch
J. Madrid-Wolff, R. Emma, A. Boniface, C. Moser
Laboratory of Applied Photonics Devices
School of Engineering
Ecole Polytechnique Fédérale de Lausanne
Lausanne 1015, Switzerland
E-mail: christophe.moser@epfl.ch
D. Loterie, P. Delrot
Readily3D SA
EPFL Innovation Park, Building A, Lausanne 1015, Switzerland

The ORCID identification number(s) for the author(s) of this article can be found under https://doi.org/10.1002/admt.202202117

[+]Present address: Shaping Matter Lab, Faculty of Aerospace Engineering, Delft University of Technology, HS Delft, 2629 Delft, The Netherlands

DOI: 10.1002/admt.202202117

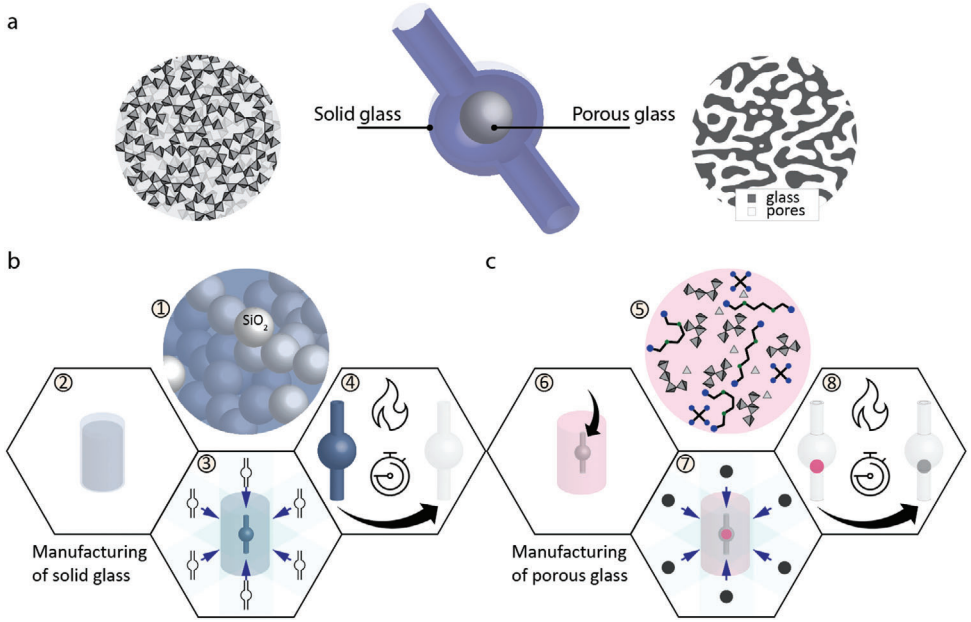

Figure 1. Schematics of the multimaterial volumetric printing of glass objects. a) Exemplary glass object consisting of a porous glass sphere encapsulated inside a dense-walled fluidic cage. The porous sphere displays a multicomponent silica-based glass composition, whereas the fluidic cage is made of pure amorphous silica glass. b,c) Sequential manufacturing steps for the fluidic cage with dense silica walls and the enclosed sphere made from multicomponent porous glass. In this workflow, the resin with silica nanoparticles (1) or phase-separating mixture (5) is placed in the transparent vial (2,6) and exposed to light projections during volumetric printing (3,7) before the final step of heat treatment to convert the polymerized resin into the final dense (4) or porous (8) glasses.

after heat treatment, whereas monomer mixtures are utilized for the polymerization of the resin under the illumination imposed by the printer. Recent work has demonstrated the fabrication of complex-shaped SiO_2-B_2O_3-P_2O_5 glasses using this light-based printing method.[2] Notably, the photo-reactive resin was found to phase separate into interpenetrating inorganic-rich and organic-rich domains during the photo-polymerization process. Such an effect was harnessed to create multicomponent glasses with complex macroscopic shapes and interconnected porosity at the nanoscale. The nanoporosity arises from the controlled thermal decomposition of the organic-rich domains of the phase-separated polymerized resin. Heat treating the printed material at higher temperatures eventually sinters the inorganic phase, leading to dense multicomponent glasses with intricate 3D geometries.[2] Because they are photo-reactive and can be designed to be transparent, resins with metal alkoxide precursors may offer a viable approach for the volumetric printing of multicomponent silica-based glasses including both dense and porous microstructures.

Here, we develop and study a multimaterial volumetric printing platform for the fast fabrication of complex-shaped glass objects with tunable chemical composition and porosity. The composition of the object is tuned through the selection of metal alkoxides added to the resin, whereas the porosity is adjusted by using resins containing either particles or metal alkoxides as inorganic precursors. First, we describe the general workflow of the process using a specific glass object as an example. This is followed by a systematic investigation of the physical and chemical properties of photo-reactive resins with varying compositions. Optimal ink formulations are finally used to print a glass-based fluidic demonstrator that combines both dense and porous features in an unique 3D filtration device.

2. Results and Discussion

The multimaterial volumetric printing (MVP) process for glasses involves the two sequential steps of 3D printing and heat treatment. By using two or more different resins and lower sintering conditions, the MVP process unlocks the fabrication of glass parts featuring both dense and porous components within the same printed object. Besides porosity, the glass composition of the object can also be deliberately tuned through the choice of the building blocks present in the resin formulation. To illustrate the technology and demonstrate these features, we select an exemplary complex glass part comprising a 3D fluidic cage enclosing a spherical nanoporous object (**Figure 1**A). The glass walls of the fluidic cage are designed to be dense and made of pure silica, whereas the encapsulated sphere is a multicomponent B_2O_3-SiO_2 glass with nanoscale porosity.

The complex glass part is manufactured by volumetrically printing first the 3D fluidic cage and then the encapsulated nanoporous sphere in a second stage. To print the fluidic cage, we selected a resin formulation consisting of amorphous silica nanoparticles suspended in a photo-curable monomer mixture (Figure 1B).[1] For volumetric printing, the fluid resin is first poured into a transparent vial and exposed to light projected from the printer while the vial is rotating at a constant speed. Upon exposure, the illuminated resin selectively polymerizes to generate an object with the desired cage geometry in ≈1 min. The polymerized nanocomposite is then carefully washed and heat treated at

temperatures up to 1300 °C to yield a dense and transparent silica glass object.

The MVP process proceeds with the fabrication of the nanoporous sphere enclosed within the fluidic cage (Figure 1C). The encapsulated sphere is printed using a phase-separating resin containing metal alkoxide inorganic precursors and a photo-curable monomer mixture.[2] To print the enclosed sphere, we place and align the fluidic cage inside the transparent vial already filled with a fluid phase-separating resin. A resin with low viscosity is crucial to ensure flow into the channel of the fluidic cage. The resin-filled object is then illuminated again with a specific light pattern to create a sphere that is large enough to remain trapped inside the previously printed part. The print is then carefully removed from the printing vial, washed, and aged to allow for the condensation reaction of the inorganic precursors. The whole assembly comprising the printed sphere within the fluidic cage is afterward heat treated at temperatures between 500 and 700 °C to generate the final multimaterial glass object. During heat treatment, the phase-separated resin is converted into a nanoporous structure with oxides given by the metal alkoxide precursors present in the initial formulation.

The formulation of the photo-curable resins is crucial for the volumetric printing of multimaterial glass objects with complex geometries at high shape fidelity and print resolution. The resin composition affects the quality of the printed parts by changing several physical and chemical properties of the photo-curable material, such as the optical transparency, the viscosity before polymerization, the polymerization behavior, and the shrinkage of the resin during heat treatment. To understand the interplay between these properties and the underlying trade-offs, we prepared and characterized the properties of silica nanoparticles and phase-separating resins with systematically controlled chemical compositions.

The nanoparticle resin comprises amorphous silica aggregates (Aerosil Ox50) suspended in a reactive organic mixture (**Figure 2a**). The mixture consists of the monomers hydroxyethylmethacrylate (HEMA) and trimethylolpropane ethoxylate triacrylate (TA) combined with the photoinitiator diphenyl(2,4,6-trimethylbenzoyl)phosphine oxide (TPO) and the polymerization-inhibitor (2,2,6,6-tetramethylpiperidin-1-yl)oxyl (TEMPO). The concentration of silica particles has a strong impact on the optical transparency and viscosity of the resin, whereas the relative weight ratio between TEMPO and TPO strongly affects the resin's polymerization behavior.

Optical transparency is key in the volumetric printing process because it directly affects the intensity of light within the illuminated resin during manufacturing. To achieve high fidelity, empirical observations have shown that the light intensity at the center of the printing vial should reach at least 75% of the intensity of the light source.[23] In particle-filled resins, the optical transparency is reduced by particle scattering events, which can be minimized by reducing the mismatch in the refractive index between the silica and the monomer mixture.[26,27] The calculated tomographic patterns used for printing can also be computationally corrected to account for scattering from the resin or attenuation from the photoinitiator.[28] While a lower index mismatch enhances light penetration, a reduction in optical transparency in resins with high particle concentrations is inevitable. High silica particle contents promote undesired scattering events but are essential to minimize shrinkage of the printed object and crack formation during heat treatment. Clearly, a trade-off exists between optical transparency and silica particle concentration. In addition to transparency, the silica content is also limited by the viscosity of the resin, which should be fluid enough to enable effective washing and removal of unreacted monomer from the as-printed parts.

To establish an optimized resin composition that balances the trade-offs of the system, we measured the optical transmittance and the relative viscosity of resins prepared with increasing concentrations of silica particles (Figure 2b). The transmittance across the resin was quantified by UV–vis spectroscopy for the wavelength range 300–500 nm, whereas the relative viscosity was determined by steady-state shear measurements in a stress-controlled rheometer. The results show the optical transmittance at 405 nm of the resin decreases from 92% to 81% as the silica particle concentration is increased from 10 to 40 vol% (Figure 2b). Such a reduction in transmittance is accompanied by a marked increase in relative viscosity from 3 to 1400. The relative viscosity was measured at 1 s^{-1} and expresses the ratio between the viscosity of the particle-filled resin and the viscosity of the pure resin (10.1 Pa.s). On the basis of these experiments, we found the silica particle concentration of 35 vol% to offer a high optical transmittance while keeping the viscosity low enough for the effective washing of the printed parts.

In addition to particle scattering, the presence of the photoinitiator also causes light attenuation by absorbing photons to generate free radicals. Although high initiator concentrations are desired to accelerate the polymerization process, such an attenuation effect sets an upper limit to the TPO content in the resin. Light transmittance measurements indicate that this upper value lies at ≈ 1 mM, since higher concentrations reduce the light below the 75% threshold for an arbitrary penetration depth of 1 cm into the resin (Figure 2c). This means that resins with 1 mM TPO are suitable for the high-resolution volumetric printing of parts with dimensions below 1 cm. Larger parts can also be printed with such resin formulation but at the expense of printing resolution.

Next to light transmittance, the polymerization behavior of the resin is the other essential parameter controlling the shape fidelity of objects manufactured via the volumetric printing process. The polymerization behavior can be expressed in terms of the polymerization speed and the induction time needed for the onset of the reaction. To achieve high shape fidelity, it is important that the polymerization is restricted to the regions of the resin that are illuminated by the printer,[29] which is experimentally observed in resins that show long induction times and fast polymerization. The long induction time ensures that only the regions illuminated for longer than a certain threshold will initiate polymerization. Fast polymerization prevents the free radicals and reactive monomers created by the incoming photons to diffuse away from the illuminated area, since a cross-linked network with higher molecular weight is quickly formed. However, induction time and reaction speed are usually found to be antagonistic properties. This trade-off calls for an optimization of the ratio between the photo-inhibitor (TEMPO) and the photoinitiator (TPO) concentrations, which controls the induction time and the polymerization speed.

The optimum ratio between photo-inhibitor and photoinitiator was established by measuring the induction time and

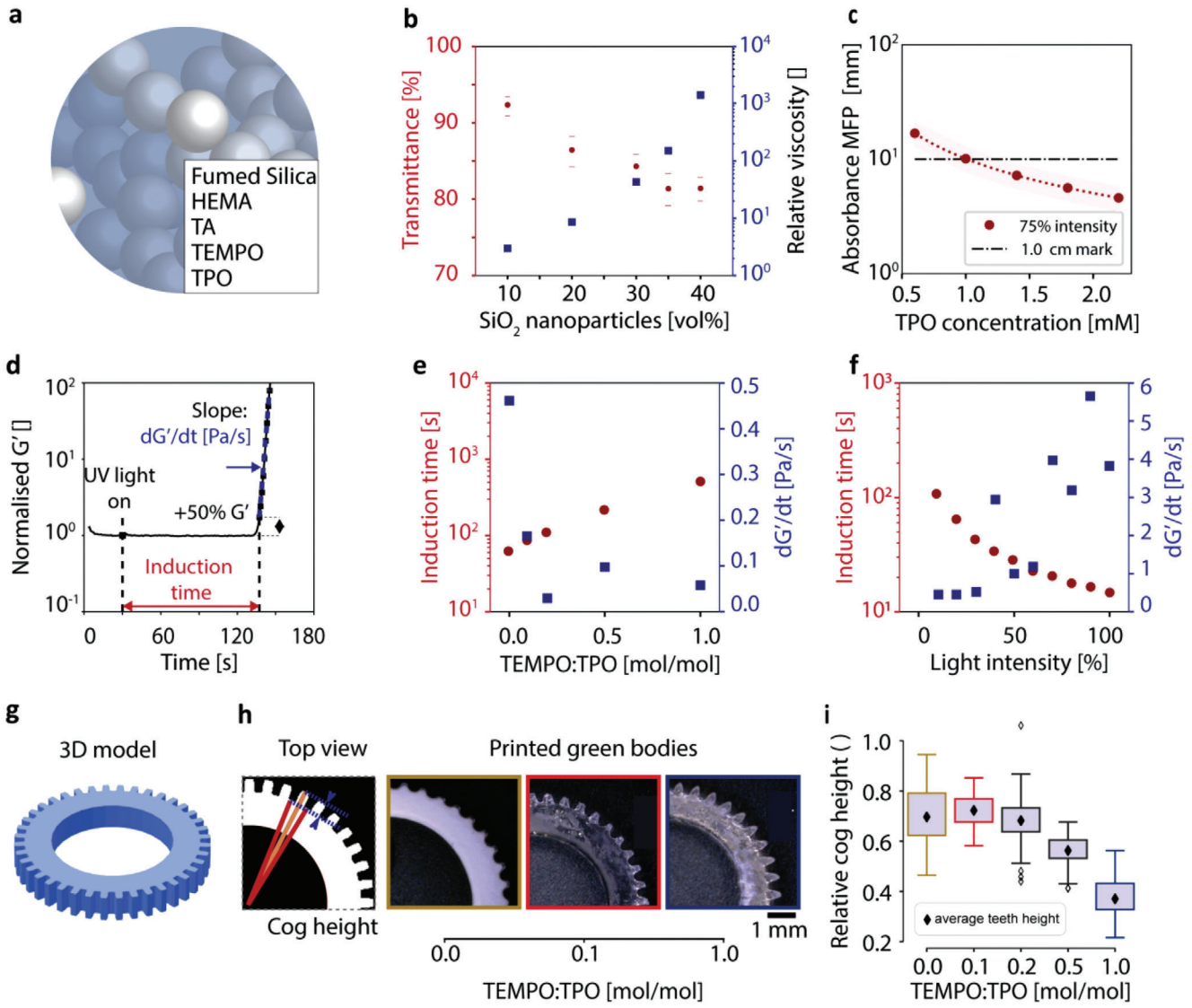

Figure 2. Optical properties, polymerization behavior, and printing of particle-filled resins. a) Schematic indicating the main constituents of the resin filled with silica nanoparticles. b) Optical transmittance and relative viscosity of the resin as a function of the concentration of silica nanoparticles. The relative viscosity corresponds to the apparent viscosity of resin at a shear rate of 11 s^{-1} relative to that of the particle-free monomer mixture. c) The penetration depth of light into the resin, expressed as absorbance mean free path (MFP), as a function of the initiator (TPO) concentration. The penetration depth is arbitrarily defined here as the depth at which the light intensity drops to 75% of the incident value. d) Evolution of the storage modulus (G') of the illuminated resin during photo-rheology experiments. The plot shows how the induction time (t_i) and the stiffness change rate (dG'/dt) are extracted from the data. e,f) Effect of the TEMPO:TPO ratio and f) light intensity on the induction time and stiffness change rate of a resin containing 35 vol% silica nanoparticles and TPO content of 1.8 mM. g) 3D model of the cog wheel used to assess the resolution and repeatability of the printing process. h) Images of the cogwheels printed with particle-filled resins of different TEMPO:TPO ratios. i) Effect of the TEMPO:TPO ratio on the average relative cog height of the printed model.

polymerization speed of resins prepared with varying TEMPO and TPO concentrations using photo-rheology. In this approach, the polymerization reaction is captured by the increase in storage modulus (G') of the resin as a function of time while the sample is illuminated with constant light intensity. The induction time is taken as the time needed for the G' value to increase by an arbitrary value of 50% (t_i), which is a proxy for the gelation point of the resin. Although the gelation time does not always coincide with the induction time of the reaction, we assume that this inflection in the stiffening curve is a good approximation for the rate of the initiation relative to the termination events involved in the polymerization process. The polymerization speed is represented by the rate of change of the modulus (dG'/dt) after the onset of gelation (Figure 2d) and expresses the rate of the propagation reaction relative to the termination reaction. The results of photo-rheology experiments with resins formulated with distinct TEMPO:TPO ratios confirm the trade-off between induction time and polymerization speed (Figure 2e). Higher TEMPO:TPO ratios represent an excess of inhibitor relative to the initiator, thus increasing the induction time at the cost of slower

polymerization speeds. Notably, the light intensity applied during printing provides an external control parameter to tune the polymerization behavior of the resin (Figure 2f). By increasing the rate of initiation relative to termination events, intense light shortens the induction time and speeds up the polymerization process.

To determine the polymerization behavior required to maximize print resolution and shape fidelity, we volumetrically printed 3D cog wheels using resin formulations with distinct TEMPO:TPO ratios (Figure 2g). Shape fidelity in this model system was quantified by the relative height of the cog, which is given by the ratio between the outer and inner radii of the wheel (Figure 2h). The average cog height provides a measure of the print accuracy, whereas the standard deviation indicates the precision of the printing process. Our experiments show that an intermediate TEMPO:TPO molar ratio of 0.1 leads to maximum resolution and repeatability, as evidenced by the highest average cog height and smallest standard deviation among all the resin compositions tested (Figure 2h,i). In the absence of TEMPO, the repeatability is poor probably due to the short induction time of the polymerization reaction. By contrast, higher TEMPO:TPO ratios in the range of 0.1–1.0 translate into lower average cog heights and a poorer resolution that likely results from a slower polymerization process.

The resin formulation design performed for the particle-filled mixture was extended to the phase-separating resins to establish a multimaterial palette for the volumetric printing platform. This was carried out by first exploring possible resin compositions leading to high optical transparency. The phase-separating resin is composed mainly of metal alkoxides as inorganic precursors mixed with photo-reactive monomers. In our exemplary formulations, polydiethoxysiloxane (PDEOS) and triethyl borate (TEB) were utilized as silicon- and boron-containing inorganic precursors, respectively. These constituents were mixed with diurethane dimethacrylate (DUDMA) and pentaerythritol tetraacrylate (PETA) as photo-reactive bifunctional and tetrafunctional monomers, respectively. The photoinitiator TPO and the photoinhibitor TEMPO were also added to the mixtures to complete the phase-separating resin formulation (**Figure 3a**).

Mixing experiments with various resin compositions were performed to identify the conditions needed to obtain miscible and transparent formulations. The composition was systematically varied by changing the weight ratio between bifunctional (DUDMA) and tetrafunctional (PETA) monomers for different relative fractions of inorganic precursors in the resin. Since high concentrations of inorganic precursors reduce the shrinkage during calcination, we focused on compositions with high contents of PDEOS and TEB. While most of the formulations were found to be immiscible at room temperature, heating the mixture to 55 °C for up to 20 min effectively increases the miscibility for most resins. The change of resin miscibility with temperature was found to be a reversible process, suggesting that heating might improve the miscibility by reversible entropic effects. Importantly, the highly transparent resins obtained clearly benefit from the absence of scattering particles in the formulations. On the basis of these experiments, we selected a composition with an appropriate balance between inorganic and organic precursors while retaining full miscibility and transparency after the heating protocol (Figure 3c).

Besides optical transparency, the selected phase-separating resin was also evaluated in terms of polymerization behavior using the photo-rheology tool previously used for the particle-filled formulations. The polymerization behavior was found to be strongly affected by the relative ratio between the photo-inhibitor and photo-initiator, as evidenced by the evolution of the storage modulus of the resin upon illumination (Figure 3d). To systematically assess the effect of these control parameters, we measured the induction time (t_i) and the stiffness change rate (dG'/dt) of resins with varying TEMPO:TPO ratios at three different TPO concentration levels. Combined, the experimental results indicate that an increase in the inhibitor:initiator ratio from 0.2 to 5.0 increases the induction time by a factor of nearly 100 and reduces the polymerization speed (dG'/dt) by 2 orders of magnitude. These trends are in line with the results obtained for the particle-filled resin and reflect the change in the balance between the initiation (propagation) and the termination reactions of the polymerization process.

To correlate this polymerization behavior with the shape fidelity of the process, we volumetrically printed a 3D helicoidal object using resin formulations with varying TEMPO and TPO concentrations (Figure 3g). Printing was performed while keeping the resin in the miscible state at 55 °C. Photographs of the resin-filled vial at the end of the printing process reveal that high fidelity is achieved with a formulation with a well-defined intermediate TEMPO:TPO ratio. Too high concentrations of the initiator (TPO) led to uncontrolled over-polymerization of the resin on the walls of the printing vial. This results from the higher doses required in resins with higher TPO concentrations, which require longer exposure time to compensate for the stronger absorbance imparted by the presence of more TPO molecules. By contrast, formulations containing high inhibitor (TEMPO) contents do not fully polymerize during the illumination process, thus resulting in incomplete printed geometries. These qualitative experiments indicate that high shape fidelity is possible if the polymerization behavior is tuned to enable induction times of ≈100 s combined with a stiffening rate of ≈0.4 Pa s^{-1}. Such behavior reflects the existence of a light dose threshold below which no reaction occurs, thus limiting the polymerization to the volumes of the resin corresponding to the desired geometry. Overall, the slower reaction kinetics of the phase-separating resin make it more challenging to achieve the high resolution obtained with the particle-filled compositions. Further research is needed in the future to better quantify the resolution of parts printed from the phase-separating formulation.

The development of particle-filled and phase-separating resins with optimal viscosity, transparency, and polymerization behavior enables volumetric printing of silica-based glass objects with multimaterial compositions and complex 3D geometries. We illustrate the capability of the MVP process by first printing a complex-shaped object in the form of a centimeter-scale swan using a particle-filled formulation (**Figure 4a**). The complex geometry of the swan is printed in less than one minute and the resulting 3D object replicates very well the original model. Despite the large dimension of the object and the 11±3% linear shrinkage during calcination and sintering, the structure maintains its integrity throughout the entire heat treatment procedure.

Printing experiments with and without TEMPO indicate that the presence of this photo-inhibitor in the particle-filled resin is

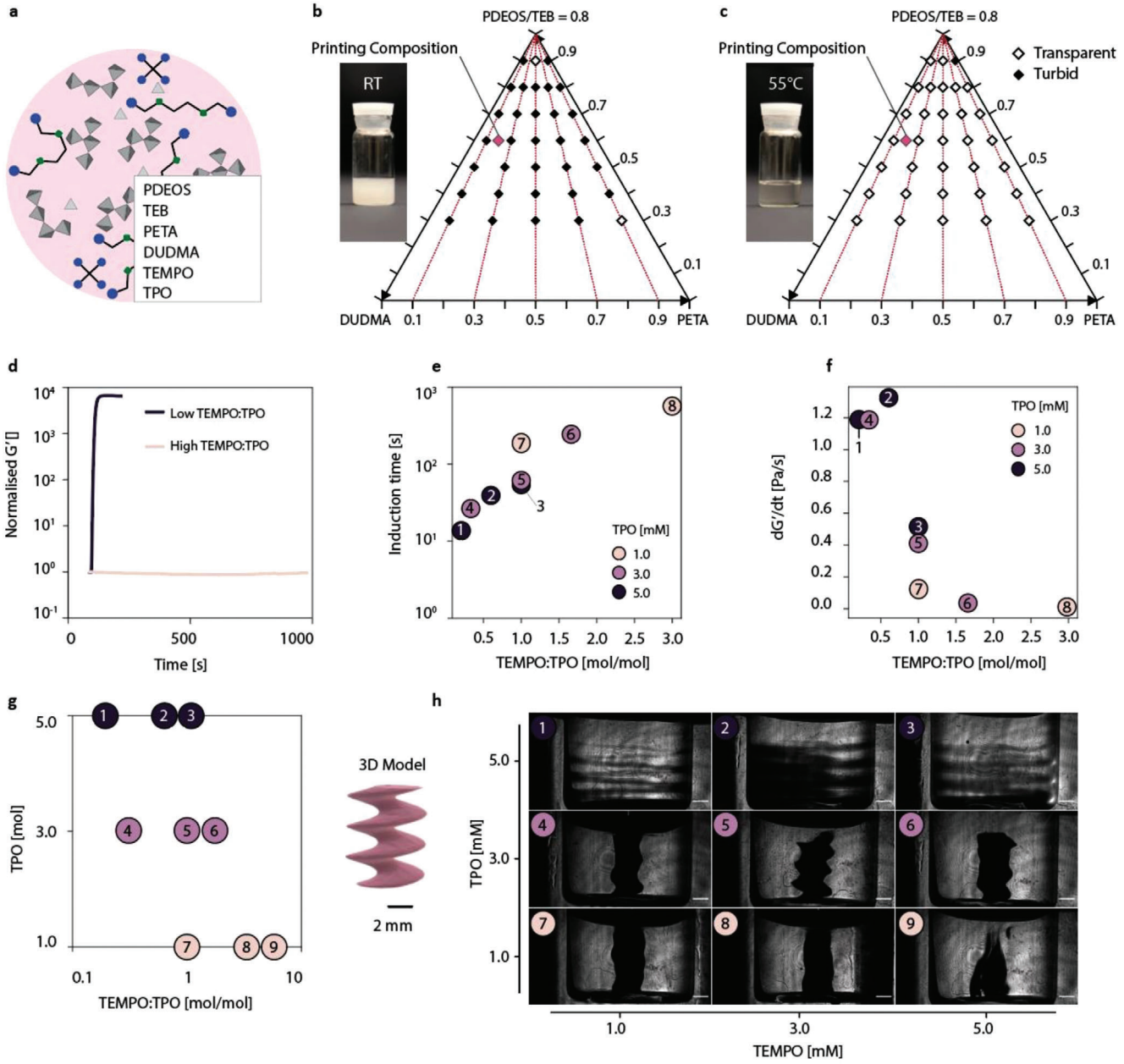

Figure 3. Transparency, polymerization behavior and shape fidelity of phase-separating resins. a) Schematic depicting the main constituents of the phase-separating resin. b,c) Ternary diagrams indicating the resin compositions that become turbid (immiscible) or optically transparent (miscible) at room temperature and after heating to 55 °C. The photographs show the phase-separating resin formulation selected for volumetric printing. d) Evolution of the storage modulus (G') of illuminated resins during photo-rheology experiments. The plot shows two examples of formulations with low and high TEMPO:TPO ratios. e,f) Effect of the TEMPO:TPO ratio on the induction time and the stiffness change rate of a selected resin containing 48 wt.% PDEOS, 12 wt.% TEB, 32 wt.% DUDMA, and 8 wt.% PETA. g) Diagram indicating the sets of compositions with different TEMPO and TPO concentrations used to test the shape fidelity of the selected resin. h) Photographs of the vials containing resins with distinct TEMPO and TPO concentrations after volumetric printing of a 3D model helicoidal structure.

essential to replicate the fine details of the swan geometry in the green part and in the final sintered structure (Figure 4b). Indeed, the finely resolved features on the swan's wings are only distinguishable in the structure printed from the formulation containing the photo-inhibitor. Such optimized formulation can eventually be used to volumetrically print silica-based glass objects in a variety of intricate geometries and shapes.

Combining the particle-filled resin with the phase-separating formulation allows us to harness the multimaterial capabilities of the proposed printing platform. Following the sequential two-step procedure, it is possible to volumetrically print the envisioned complex glass object comprising a porous borosilicate sphere entrapped inside a 3D fluidic cage with silica-dense walls (Figure 4d). The resulting object displays multimaterial,

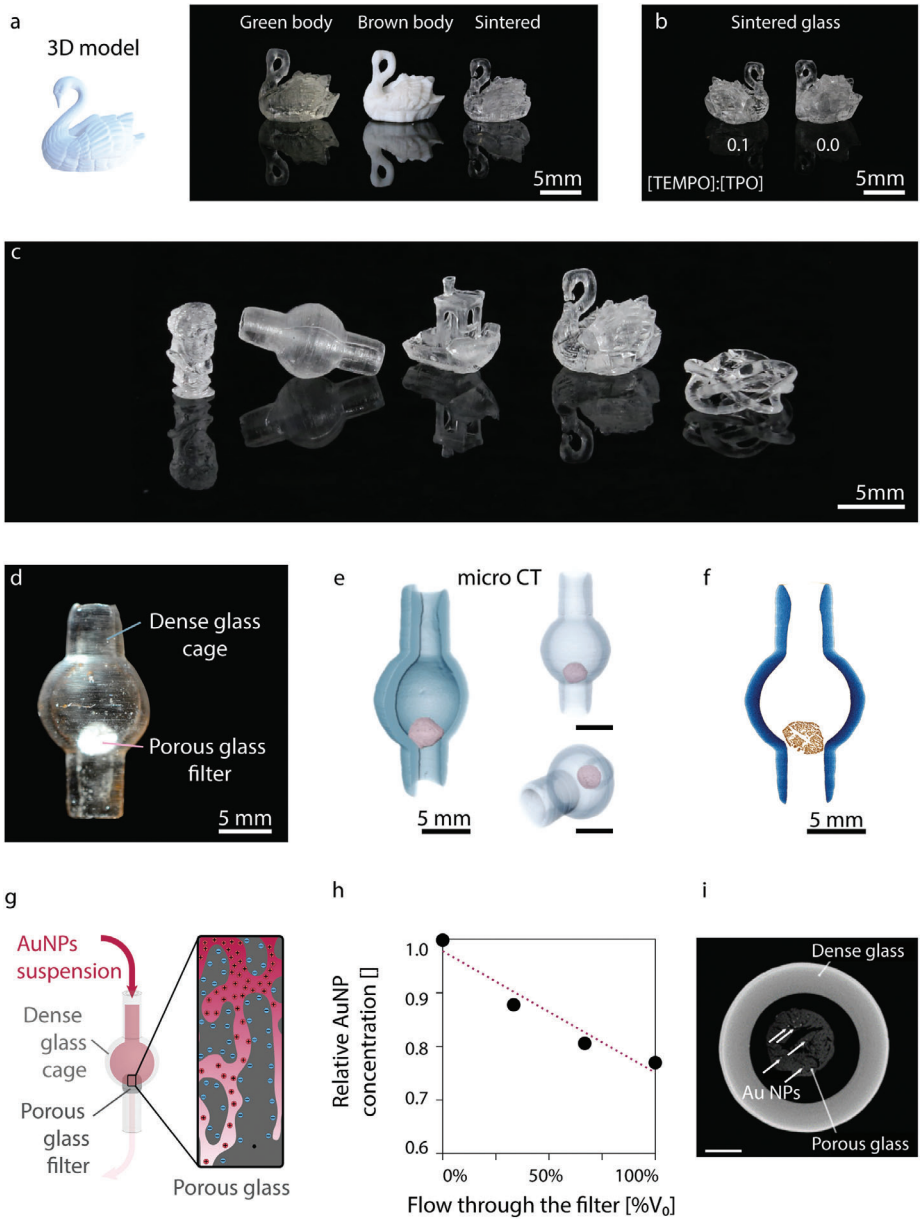

Figure 4. Multimaterial volumetric printing of complex and functional glass objects. a) Photographs of a 3D swan-shaped object at the different stages of the manufacturing process using a particle-filled resin. b) Fine-scale resolution of the swan-shaped glass objects printed with the optimal amount of polymerization inhibitor (TEMPO) compared to a sample printed without the TEMPO. c) Complex-shaped glass objects obtained by printing, calcination, and sintering of a particle-based resin containing 52.2 wt.% silica, 31 wt.% HEMA, 16.8 wt.% triacrylate, 0.18 mM TEMPO, and 1.8 mM TPO. d) 3D fluidic cage with entrapped porous sphere fabricated by multimaterial volumetric printing of particle-filled and phase-separating resins. e,f) Micro-computed tomography data shows a reconstructed 3D image and a cross-section of the glass object comprising a borosilicate porous sphere entrapped in a cage with dense silica walls. g) Filtration of nanoparticles by flowing a suspension of gold colloids through the fluidic glass cage. h) The relative concentration of gold nanoparticles in the filtrate as a function of the volume of suspension filtrated relative to the total initial volume (V_0). i) Microcomputed tomography image of the multimaterial glass object indicating the entrapment of the gold nanoparticles within the interconnected nanoporosity of the enclosed borosilicate sphere.

microstructural, and geometrical features that cannot be reconciled in the same part using conventional glass manufacturing processes. To characterize the structure of this complex object, we performed microcomputed tomography (microCT) of the sample and created 3D reconstructions from the obtained images (Figure 4e,f).

The reconstructed 3D object reveals that the entrapped sphere features a slightly oblate shape, which probably results from the focusing effect in the proximity of the cage's walls. Cross-sections of the structures show that the long axis of the sphere is sufficiently large to prevent it from escaping the cage. Closer inspection of the sphere indicates the presence of a microscale inner

pore that likely forms during the removal of the organic phase of the polymerized resin during the calcination process. Importantly, the formation of such pores does not affect the shape and mechanical integrity of the sphere, allowing it to be used as a high-surface-area porous substrate entrapped in the fluidic cage.

To demonstrate the functionality of the sphere-in-a-cage glass object, we conducted a simple filtration experiment in which the porosity of the encaged sphere is exploited to separate 36 ± 2 nm gold particles dispersed as a model colloid in an aqueous suspension (Figure 4g). Separation is favored by adsorbing positively charged cysteamine on the gold nanoparticles, so as to promote electrostatic interactions with the negatively charged surface of the silica sphere. Experiments are performed by flowing the gold suspension through the fluidic cage and collecting the filtrate for analysis. To quantify the effectiveness of the filtration process, we measured the concentration of gold nanoparticles in the filtrate using UV–vis spectroscopy.

The sphere-in-a-cage object was found to effectively separate the gold nanoparticles from the water phase by flowing the suspension through the fluidic device. The gold content left in the filtrate decreases linearly with the volume of the filtrated suspension, indicating the positive effect of the electrostatic interactions between the particles and the porous glass sphere. MicroCT images of the device after the filtration experiment show that the gold nanoparticles are entrapped within the inner nanopores of the sphere. This confirms the interconnected nature of the nanoporosity generated upon calcination of the phase-separated resin, which is essential to provide a high surface area for the filtration process. Combined with the chemical and thermal stability of silica glass, such interconnected nanoporosity makes our multimaterial glass object attractive for membrane-based separation technologies.

3. Conclusion

Volumetric printing of resins loaded with silica particles or metal alkoxides enables the manufacturing of silica-based glasses featuring complex 3D geometry combined with compositional and microstructural control. Particle-laden resins are suitable for the fabrication of glass structures with dense silica walls, whereas resins with the metal alkoxides can be used to tune the chemical composition and local porosity of the glass. The design of the resin formulation is key to volumetrically print structures with high shape fidelity. By tuning the concentration of particles or molecular inorganic precursors, it is possible to formulate resins with the optical transparency required for the volumetric printing process. To print such resins into high-fidelity structures, the induction time and polymerization speed need to be optimized through the concentrations of photo-initiator and photo-inhibitor. Under optimal conditions, the initiation, propagation, and termination reactions of the polymerization process reach a balance that allows for controlled cross-linking of the resin within the desired projected volume. The combination of resins with particles and molecular precursors enables the multimaterial volumetric printing of 3D glass objects with unprecedented control over the geometry, porosity, and chemical composition of the printed structure. This printing platform can open new opportunities for the fabrication of complex glass structures for potential microfluidic and biomedical applications.

4. Experimental Section

Particle-Filled Resin: The particle-filled resin was designed for computed axial lithography based on the formulations originally developed by Wozniak et al.[7,30] and Kotz et al.[1] 65 vol% of hydroxyethylmethacrylate (HEMA, Sigma–Aldrich) was first mixed with 35 vol% trimethylolpropane ethoxylate triacrylate (TA, Sigma–Aldrich). Next, amorphous silica nanopowder (Aerosil OX50, Evonik, Germany) was added in small amounts to the mixture using a laboratory stirrer (type R 1303, IKA, Germany). The dispersion was then mixed for 3 min at 1200 rpm and degassed for 5 min at 1400 rpm using a planetary mixer (ARE 250, Thinky, USA). Finally, the initiator diphenyl-(2,4,6-trimethylbenzoyl)-phosphinoxid (TPO, Sigma–Aldrich) and, if needed, the inhibitor 2,2,6,6-tetramethylpiperidine 1-oxyl (TEMPO, Sigma-Aldrich) was added using a concentrated HEMA stock solution as the vehicle. Before printing, the second and last step of mixing and degassing was performed in a planetary mixer (Mazerustar KK-250SE, Kurabo, Japan).

Phase-Separating Resin: The phase-separating resin was designed based on the original formulation described by Moore et al.[2] The resin comprised a mixture of 40 wt.% of a monomer phase and 60 wt.% of glass-forming precursors. The monomer phase consisted of 80wt.% diurethane dimethacrylate (DUDMA, Sigma–Aldrich) and 20wt.% pentaerythritol tetraacrylate (PETA, abcr GmbH). The 60 wt.% glass-forming phase contained a blend of 80 wt.% poly(diethoxysiloxane) (PDEOS, 45–47% SiO2, abcr GmbH) and 20 wt.% triethyl borate (TEB, Sigma–Aldrich) as molecular precursors for silicon and boron glass-forming oxides, respectively. The desired amount of diphenyl(2,4,6-trimethylbenzoyl)phosphine oxide (TPO, 97%, Sigma–Aldrich) and 2,2,6,6-tetramethylpiperidine 1-oxyl, free radical (TEMPO, Sigma Aldrich) was added to the formulation to control the polymerization behavior of the resin.

Rheological Characterization: The rheological behavior of the resins was characterized on a stress-controlled rheometer (MCR 302 Anton-Paar, Graz, Austria) equipped with a cone-plate geometry (CP25, diameter: 24.98 mm, gap: 106 µm, and angle: 2°). Steady-shear measurements were performed at 25 °C by applying a ramp-up and ramp-down protocol with shear rates between 0.1 and 100 1 s^{-1} on a logarithmic scale. Amplitude sweeps under oscillatory mode were performed with an angular frequency of 1 Hz and shear strain values of 0.1 up to 100%.

Photorheological Characterization: Photorheology experiments were carried out on a stress-controlled rheometer (MCR 301, Anton Paar, Graz, Austria). The setup was equipped with a 6 mm thick glass base and a UV curing station (Omnicure Series1000, Lumen Dynamics) in combination with a 400–500 nm filter. In the described arrangement, the setup had a maximum output power of 12.2 mW cm^{-2}. For the particle-filled resin, oscillatory measurements were performed at 25 °C by applying a 1% strain amplitude and frequency of 1 Hz using a cone-plate geometry (CP25). The gap size was set to 173 µm and data were acquired every second. The resins were pre-sheared and equilibrated for 30 s before the UV light was turned on. The set of measurements with distinct TEMPO:TPO ratios was performed at 2.44 mW cm^{-2} (20% of output power capacity). For the phase-separating resin, oscillatory measurements were performed at 25 °C by applying a 1% strain amplitude and 1 Hz frequency in a plate-plate geometry (PP50) with a 50 µm gap. Data points were acquired at a rate of 0.5 Hz. The phase-separating samples were pre-sheared and equilibrated for 60 s before the UV light was turned on. The measurements were carried out at the full power capacity of 12.2 mW cm^{-2}.

Optical Transmittance of Resins: The light transmittance of the particle-filled resin was measured with a UV–vis spectrometer (Cary 50, Varian, Australia) using a scan rate of 60 nm min^{-1}. The resin was carefully poured in a 10 mm plastic cuvette making sure no air bubbles were incorporated in the sample. For each analysis, a background measurement was performed before acquiring the spectra between 340 and 420 nm. Transmittance at 405 nm was then reported.

Volumetric Printing: A volumetric 3D printer previously described in the literature[23] was used in this work (Figure S1, Supporting Information). In this setup, UV light emitted from 4 laser diodes with a wavelength of $\lambda = 405$ nm was coupled into a multimode fiber and expanded to fill a Digital Micromirror Device (DMD, VIS-7000, Vialux, Germany) through

two cylindrical lenses. Light patterns arising from the interaction between the emitted light and the DMD were used for the tomographic backprojection. Patterns were projected by a pair of achromatic lenses into a glass vial containing the reactive resin, which was mounted on a rotating stage. The vial itself was immersed in a square container filled with a refractive-index-matching bath to remove the lensing effects coming from the round walls of the vial. A camera recorded the progress of the print in the vial by imaging the sample with an orthogonal 671 nm expanded laser beam as described in recent work.[28] The patterns for the tomographic backprojection were computed following a previously reported algorithm.[23] Briefly, the STL file of the 3D object was voxelized and its Radon transform was calculated with respect to the axis aligned with the vial centerline. Next, the Fourier transform of the sinogram was calculated in combination with a ramp filter to compensate for the over-sampling of the low spatial frequencies. Finally, the inverse Fourier transform of these patterns was calculated to recover the light pattern to project into the resin vial. Additional corrections to compensate for the change in optical properties of the phase-separating resin were applied following the reported procedures.[28]

Post-Processing of Printed Parts—Particle-Filled Resin: The objects printed using the particle-filled formulation were recovered from the glass vial and immersed for 3 min in a 1:1 mixture by volume of water:methanol to remove residual unreacted resin. For samples containing cavities or channels, an air gun was used to free the voids from the viscous unpolymerised material. The green bodies were then left to dry in air at room temperature until residual solvent evaporated, leaving them free of any unreacted monomers.

Post-Processing of Printed Parts—Phase-Separating Resin: The objects printed using the phase-separating resin were transferred to a basic bath containing 65 wt.% of a solution of tetrabutylammonium hydroxide in ethanol and 35 wt.% water at pH 10 for 24 h. Subsequently, the printed samples were left drying in a closed container with the saturated atmosphere of a basic bath for an additional 24 h. The saturated atmosphere was created by placing a vial with this basic bath within the drying container. Finally, the objects were left drying in an ambient atmosphere for another day before calcination in an electrical furnace.

Thermal Calcination and Sintering—Particle-Filled Resin: Calcination of the printed and rinsed green bodies was performed in a muffle furnace (Nabertherm LT, Germany) under atmospheric conditions by applying a heating rate of 0.5 °C min^{-1}. During this heat cycle, isotherm holds were performed at 120, 320, and 600 °C for 2, 4, and 2 h, respectively (Figure S2, Supporting Information). This calcination protocol was established based on the thermal gravimetric analysis of the particle-filled resin (Figures S3 and S4, Supporting Information). The parts were afterward sintered at 1300 °C at a pressure between 10^{-5} and 10^{-6} bar in a tube furnace (HTRH 70- 600/18, Nabertherm, Germany) using a heating rate of 3 °C min^{-1}. Prior to sintering the calcined (brown) samples, the furnace was kept at room temperature for 2 h to ensure high vacuum. The heating profiles optimized in the work of Kotz et al.[1] were utilized for the sintering process.

Thermal Calcination and Sintering—Phase-Separating Resin: Objects printed with the phase-separating resin were calcined in a muffle furnace (Nabertherm LT, Germany) under atmospheric conditions with a heating rate of 0.4 °C min^{-1}. Isotherms at 250 °C for 6 h and at 700 °C for 4 h were performed to enable calcination of the organic phase and the generation of nanoporosity in the final glass (Figure S5, Supporting Information). This calcination protocol was established based on the thermal gravimetric analysis of the phase-separating resin (Figure S4, Supporting Information).

Microcomputed Tomography of Glass Device: Printed and heat-treated glass objects were imaged using a 160 kV X-ray transmission tomography (Hamatsu, Japan) with voxel sizes of 8.4 µm × 8.4 µm × 8.4 µm. 3D visualization of the pieces was achieved using the software Fiji-ImageJ[31] and Avizo (ThermoFischer).

Synthesis of Gold Nanoparticles: Positively charged gold nanoparticles were synthesized following the procedure described by Niidome et al.[32] In this synthesis, $AuCl_3$ was reduced in the presence of $NaBH_4$ and 2-aminoethanethiol. To this end, 400 µL of 213 mM 2-aminoethanethiol was added to 40 mL of 1.42 mM $AuCl_3$. After stirring for 20 min, 10 mL of 10 mM $NaBH_4$ was added and further stirred for 10 min. Finally, the clear wine-red sample was stored in a fridge at 5 °C and used within 2 months.

Filtration Experiments: The filtering efficiency of the sphere-in-a-cage glass device (Figure 4g–i) was assessed by quantifying the removal of positively charged gold nanoparticles (AuNP) from an aqueous solution as it passed through the fluidic device. The suspension of gold nanoparticles was flowed through the device using a peristaltic pump (AL-9000, World Precision Instruments, Germany). Using a flow rate of 5 mL per minute, the particles were continuously filtered by the porous sphere in a closed-loop circulatory setup. Samples of 200 µL were taken every 20 s to quantify the amount of gold particles left in the suspension. This was possible by measuring the change in absorbance of the samples using a UV–vis spectrometer (Cary 50, Varian, Australia).

Characterization of Print Fidelity: To assess the fidelity of the printing process, each gear was printed with a different TEMPO concentration and imaged under an optical microscope (VHX-5000, Keyence VHX-5000, Japan). The cog heights were measured with Fiji-ImageJ.[31]

Phase Diagrams of Phase-Separating Resins: The ternary phase diagrams depicting the miscibility of the resin mixture (Figure 3b,c) were constructed by mixing known amounts of resin components and observing for turbidity at room temperature. Next, the same specimen was heated to 55 °C and inspected for turbidity. For each specimen, the total sample volume was 2 mL.

Supporting Information

Supporting Information is available from the Wiley Online Library or from the author.

Acknowledgements

L.B. and J.M.W. contributed equally to this work. LB and AS gratefully acknowledge Univerre Pro Uva SA for financially supporting this research. The study also benefited from support from ETH Zürich. J.M.W, A.B., and C.M. acknowledge funding by the Swiss National Science Foundation under project number 196971 – "Light-based Volumetric printing in scattering resins."

Open access funding provided by Eidgenossische Technische Hochschule Zurich.

Conflict of Interest

DL and PD are shareholders and employees of Readily3D SA. CM is a shareholder of Readily3D SA.

Data Availability Statement

The data that support the findings of this study are available from the corresponding author upon reasonable request.

Keywords

3D printing, additive manufacturing, digital fabrication, multicomponent oxides, silicates

Received: November 29, 2023
Published online: February 21, 2024

[1] F. Kotz, K. Arnold, W. Bauer, D. Schild, N. Keller, K. Sachsenheimer, T. M. Nargang, C. Richter, D. Helmer, B. E. Rapp, *Nature* **2017**, *544*, 337.

[2] D. G. Moore, L. Barbera, K. Masania, A. R. Studart, *Nat. Mater.* **2020**, *19*, 212.
[3] J. Klein, M. Stern, G. Franchin, M. Kayser, C. Inamura, S. Dave, J. C. Weaver, P. Houk, P. Colombo, M. Yang, N. Oxman, *3D Print. Addit. Manuf.* **2015**, *2*, 92.
[4] D. T. Nguyen, C. Meyers, T. D. Yee, N. A. Dudukovic, J. F. Destino, C. Zhu, E. B. Duoss, T. F. Baumann, T. Suratwala, J. E. Smay, R. Dylla-Spears, *Adv. Mater.* **2017**, *29*, 1701181.
[5] C. Liu, B. Qian, X. Liu, L. Tong, J. Qiu, *RSC Adv.* **2018**, *8*, 16344.
[6] I. Cooperstein, E. Shukrun, O. Press, A. Kamyshny, S. Magdassi, *ACS Appl. Mater. Interfaces* **2018**, *10*, 18879.
[7] M. Wozniak, T. Graule, Y. de Hazan, D. Kata, J. Lis, *J. Eur. Ceram. Soc.* **2009**, *29*, 2259 .
[8] X. Wen, B. Zhang, W. Wang, F. Ye, S. Yue, H. Guo, G. Gao, Y. Zhao, Q. Fang, C. Nguyen, X. Zhang, J. Bao, J. T. Robinson, P. M. Ajayan, J. Lou, *Nat. Mater.* **2021**, *20*, 1506.
[9] Hong, P. A. R. Ye, D. A. Loy, R. G. Liang, *Optica* **2021**, *8*, 904.
[10] Z. H. Hong, P. R. Ye, D. A. Loy, R. G. Liang, *Adv. Sci.* **2022**, *9*, 10.
[11] J. Luo, L. J. Gilbert, C. Qu, R. G. Landers, D. A. Bristow, E. C. Kinzel, *J. Manuf. Sci. Eng.* **2017**, *139*, 061006.
[12] J. F. Destino, N. A. Dudukovic, M. A. Johnson, D. T. Nguyen, T. D. Yee, G. C. Egan, A. M. Sawvel, W. A. Steele, T. F. Baumann, E. B. Duoss, T. Suratwala, R. Dylla-Spears, *Adv. Mater. Technol.* **2018**, *3*, 1700323.
[13] C. Liu, B. Qian, R. Ni, X. Liu, J. Qiu, *RSC Adv.* **2018**, *8*, 31564.
[14] F. Kotz, A. S. Quick, P. Risch, T. Martin, T. Hoose, M. Thiel, D. Helmer, B. E. Rapp, *Adv. Mater.* **2021**, *33*, 2006341.
[15] R. Arita, M. Iijima, Y. Fujishiro, S. Morita, T. Furukawa, J. Tatami, S. Maruo, *Commun. Mater.* **2020**, *1*, 30.
[16] Y. Xu, Y. Li, N. Zheng, Q. Zhao, T. Xie, *Nat. Commun.* **2021**, *12*, 4261.
[17] B. Nan, P. Gołębiewski, R. Buczyński, Galindo-Rosales, J. M. F. Ferreira, *Materials* **2020**, *13*, 1636.
[18] T. Doualle, J. C. Andre, L. Gallais, *Opt. Lett.* **2021**, *46*, 364.
[19] P. Cai, L. Guo, L. Liu, Q. Zhang, J. Li, Q. Lue, *Ceram. Int.* **2022**, *48*, 55.
[20] A. De Marzi, G. Giometti, J. Erler, P. Colombo, G. Franchin, *Addit. Manuf.* **2022**, *54*, 102727.
[21] M. Shusteff, A. E. M. Browar, B. E. Kelly, J. Henriksson, T. H. Weisgraber, R. M. Panas, N. X. Fang, C. M. Spadaccini, *Sci. Adv.* **2017**, *3*, eaao5496.
[22] B. E. Kelly, I. Bhattacharya, H. Heidari, M. Shusteff, C. M. Spadaccini, H. K. Taylor, *Science* **2019**, *363*, 1075.
[23] D. Loterie, P. Delrot, C. Moser, *Nat. Commun.* **2020**, *11*, 852.
[24] M. Kollep, G. Konstantinou, J. Madrid-Wolff, A. Boniface, L. Hagelüken, P. V. W. Sasikumar, G. Blugan, P. Delrot, D. Loterie, J. Brugger, C. Moser, *Adv. Eng. Mater.* **2022**, *24*, 2101345.
[25] J. T. Toombs, M. Luitz, C. C. Cook, S. Jenne, C. C. Li, B. E. Rapp, F. Kotz-Helmer, H. K. Taylor, *Science* **2022**, *376*, 308.
[26] P. N. Bernal, M. Bouwmeester, J. Madrid-Wolff, M. Falandt, S. Florczak, N. G. Rodriguez, Y. Li, G. Größbacher, R.-A. Samsom, M. van Wolferen, L. J. W. van der Laan, P. Delrot, D. Loterie, J. Malda, C. Moser, B. Spee, R. Levato, *Adv. Mater.* **2022**, *34*, 2110054.
[27] T. Boothe, L. Hilbert, M. Heide, L. Berninger, W. B. Huttner, V. Zaburdaev, N. L. Vastenhouw, E. W. Myers, D. N. Drechsel, J. C. Rink, *eLife* **2017**, *6*, e27240.
[28] J. Madrid-Wolff, A. Boniface, D. Loterie, P. Delrot, C. Moser, *Adv. Sci.* **2022**, *9*, 2105144.
[29] C. M. Rackson, K. M. Champley, J. T. Toombs, E. J. Fong, V. Bansal, H. K. Taylor, M. Shusteff, R. R. McLeod, *Addit. Manuf.* **2021**, *48*, 102367.
[30] M. Wozniak, Y. de Hazan, T. Graule, D. Kata, *J. Eur. Ceram. Soc.* **2011**, *31*, 2221.
[31] J. Schindelin, I. Arganda-Carreras, E. Frise, V. Kaynig, M. Longair, T. Pietzsch, S. Preibisch, C. Rueden, S. Saalfeld, B. Schmid, J.-Y. Tinevez, D. J. White, V. Hartenstein, K. Eliceiri, P. Tomancak, A. Cardona, *Nat. Methods* **2012**, *9*, 676.
[32] T. Niidome, K. Nakashima, H. Takahashi, Y. Niidome, *Chem. Commun.* **2024**, 1978.